I N F O R M A T I K

Axisymmetric Reconstruction and 3D Visualization of Bipolar Planetary Nebulae

Marcus Magnor

MPI–I–2004–NWG3–001 April 2004

FORSCHUNGSBERICHT RESEARCH REPORT

M A X - P L A N C K - I N S T I T U T
F Ü R
I N F O R M A T I K

Stuhlsatzenhausweg 85 66123 Saarbrücken Germany

Authors' Addresses

Marcus Magnor
Max-Planck-Institut für Informatik
Stuhlsatzenhausweg 85
66123 Saarbrücken
magnor@mpi-sb.mpg.de

Abstract

Determining the true shape of distant astronomical objects is a challenging task, given that terrestrial observations provide only one viewpoint. For this task, bipolar planetary nebulae are interesting objects of study because of their pronounced axial symmetry. Making use of these properties, we present a technique to automatically recover the axisymmetric structure of bipolar planetary nebulae from conventional two-dimensional images. With GPU-based volume rendering driving a non-linear optimization, we estimate the nebula's local emission density as a function of its radial and axial coordinates, and we recover the orientation of the nebula relative to Earth. The optimization refines the nebula model and its orientation by minimizing the differences between the rendered image and the original astronomical image. The resulting nebula model enables realistic 3D visualizations, e.g. for educational purposes in planetarium shows.

Keywords

volumetric modeling, inverse rendering, volume rendering, volume reconstruction, planetary nebulae

1 Introduction

Planetary nebulae (PNe)[1] are among the esthetically most appealing objects in the night sky, due to their diversity and colorful appearance. While it was soon realized that we are observing 2D projections of 3D volumes of glowing gas, the actual spatial structure of PNe has long been an object of inquiry. It was not until the second half of the 20th century that, based on earlier morphological classifications [1], qualitative models were proposed to explain the general appearance of PNe [2, 3, 4]. These simple models are able to qualitatively describe observed PN shapes. However, they cannot reflect the true three-dimensional structure of actual planetary nebulae.

In this paper, we present a volume modeling technique coined *constrained inverse volume rendering* (CIVR) that recovers the actual structure of bipolar planetary nebula from conventional images. Based on fast volume rendering using PC graphics hardware, we synthesize realistic views from a very general PN model. An optimization algorithm varies the model's emission distribution parameters and compares the rendered model to the actual image until the rendered model matches the observed image. To make the problem well-posed and at the same time obtain only physically plausible results, we constrain the reconstruction process by exploiting the axisymmetric nature of bipolar PNe, which is both physically derivable and observationally validated. The reconstructed volumetric structure of planetary nebulae enables creating realistic views of these interesting astronomical objects from arbitrary vantage points in space, e.g. in planetarium shows and for educational purposes.

In the following Section, we review previous work related to our contribution. After an introductory overview of the fundamental physics of PNe in Sect.3, we describe our constrained inverse volume rendering approach in Sect.4. Sect.5 illuminates the practical steps in reconstructing planetary nebulae. Results are presented in Sect.6. We discuss our method and its limitations as well as validate it in Sect.7, before we conclude in Sect.8 mentioning potential astrophysical research applications and giving an outlook on future possibilities.

[1]We will use "PN" and "PNe" to refer to planetary nebulae in the singular and plural, respectively.

2 Related Work

The presented volumetric modeling technique heavily relies on recent advances in visualization and graphics research. The term *inverse volume rendering* was first employed by Curless and Levoy [5] to refer to updating volume data from range images. In Ref. [6], the same term refers to a re-projection technique in CT reconstruction. Our use of the term is derived from Marschner's PhD thesis [7] in which he introduces the term *inverse rendering* to denote the idea of reconstructing scene properties from image data via computer graphics techniques.

The volume modeling approach we present is based on the ability to perform *volume rendering* [8] very efficiently on modern graphics hardware. Cabral et al. [9] demonstrate how to perform efficient volume rendering using texture mapping hardware, a fundamental technique that is still applicable to today's programmable graphics architectures [10]. For purely self-emitting volumes, Cabral's slicing technique directly yields correct rendering results [11].

While spectacular 3D fly-throughs of astronomical objects can be experienced in many planetariums, these animations are almost always purely artistic pieces of work. One notable exception is the effort by Nadeau et al. [12] who use massive computational power to create scientifically accurate views of the Orion nebula for the Hayden Planetarium in New York [13]. For their visualizations, they rely on a 3D model of the Orion nebula that was determined by astronomers from decades of observational data [14]. Our method, in contrast, simultaneously reconstructs the 3D volume model and visualizes it, albeit for a different class of astronomical objects: planetary nebulae (PNe).

In astrophysics, a large body of literature deals with the morphology and shape of PNe. Curtis [1] classified the planetary nebulae known at his time based on their visual appearance into different classes. Khromov and Kohoutek [2] qualitatively described the diversity in PN appearance as an effect of nebula orientation from one generic 3D shape. Balick [3] and Kwok [15] introduced the interacting-winds theory to explain the physical processes leading to the 3D structure of PNe. Making use of involved astronomical observation techniques, 3D gas velocities have been directly measured and the three-dimensional gas distribution inferred for a handful of PNe by Sabbadin et al. [16, 17] and Saurer [18]. To investigate the physical processes leading to the observed PN structures, gas-kinetic and photoionization simulations have been conducted, e.g. by Mellema and Frank [19], Kimeswenger et al. [20] and Ercolano et al. [21]. The simulation results qualitatively confirm observational findings. Limited computational capacity, however, currently prevents the simulation parameters to be driven by observational data, and visual correspondence between simulation results and individual planetary nebulae has yet to be established.

3 Planetary Nebulae

In the following, we give a brief explanatory overview of the main physical processes that lead to the visual appearance of bipolar PNe. For a more thorough introduction to the physics of gaseous nebulae in general and PNe in specific, we recommend the classic books on the topic by Osterbrock [22] and Kwok [23].

Despite their name, planetary nebulae are of extra-solar origin: they constitute the last episode in the lives of most stars. On astronomical scales, they are extremely short-lived, existing only for a few tens of thousands of years before they fade away, which is why only about 1,500 have been discovered in our Galaxy so far. Owing to their great distances from earth, they are small, spanning at most a few arc minutes in the sky, and dim. For the work presented here, we rely on publicly available images that have been recorded with the Hubble Space Telescope [24] and the Nordic Optical Telescope at Teneriffe, Canary Islands [25].

3.1 Photo-ionization

When a star of initially less than eight times the mass of our Sun nears its end of energy production, a strong wind blows off its surface, carrying substantial amounts of stellar matter into space and exposing deeper, hotter regions of the star. This wind consists mainly of hydrogen but also of other elements that were previously synthesized within the star's core. At the same time, the central star contracts, increasing its surface temperature even further.

Following Wien's law for blackbody radiation [22], with rising surface temperature the star emits more high-energy ultra-violet (UV) photons. Once the star emits enough UV photons carrying sufficient energy to ionize hydrogen (13.6 eV, a wavelength of 91nm), the ejected hydrogen gas becomes completely photo-ionized, i.e. essentially all hydrogen atoms are being separated into free electrons and hydrogen ions (protons). Within this plasma, both constituents frequently recombine to form neutral hydrogen atoms again. These newly formed atoms are typically in an excited state, however, from which they return to the ground state via a cascade of energy transitions, before another UV photon ionizes the atom again. Each transition during this cascade is accompanied by the emission of a photon of a distinct wavelength. It is these emission line photons that we observe and that are responsible for the nebula's characteristic color.

Besides hydrogen, the other chemical elements in the nebula are also in ionized states and emit photons at characteristic wavelengths. Thus, images recorded at different wavelengths enable astronomers to identify different elements in different regions of a nebula, Fig.3.

For most (mature) PNe, the central star's UV photon flux is more than sufficient to photo-ionize all gas that was previously blown off the star. Since, in addition, there is typically very little light-absorbing dust in the stellar wind, we observe the entire mass of ejected gas as a glowing volume in space, with virtually none of the visible-wavelength photons being absorbed within the nebula [23].

3.2 Axisymmetry

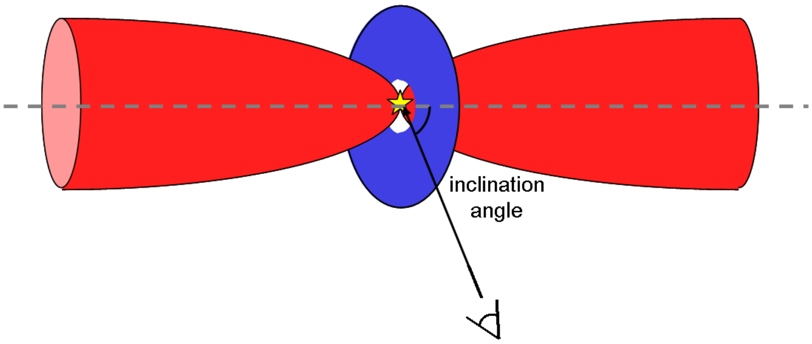

Figure 1: Interacting winds theory: During its lifetime, a torus of dense, slowly outward moving gas gathers in the equatorial plane of the central star (blue). At the end of its life, the star suddenly blows off gas at a much higher rate. When this fast wind hits the inner boundary of the old gas masses, the fast-moving gas is re-directed and escapes as two jets in opposite, polar directions (red).

As described above, PNe glow because gas previously ejected from the central star is being ionized by the star's intense UV radiation. Photo-ionization alone, however, cannot explain the bipolar shape of PNe since the central star certainly radiates isotropically into all directions. Instead, it is the non-uniform spatial distribution of the gas that is responsible for the bipolar appearance of most PNe.

A classification scheme for PNe based on visual morphology was proposed by Curtis early in the 20th century [1]. In the 1960s, it became clear that the various apparent forms of most PNe can be qualitatively explained by one common generic 3D shape viewed from Earth at different orientations [2]. While this phenomenological model was motivated by observational data, it did not explain the physical processes leading to the shape. Kwok [15] and Balick [3] finally proposed a mechanism that explains the observed gas distribution in PNe, Fig.1; their *interacting winds theory* starts with the premise that prior to its final stage, the star has already been blowing off gas, but at a much slower speed. Due to the star's rotation and the resulting centripetal force, this moderate wind blew off and aggregated mostly in the star's equatorial plane. As the rate of gas discharge increases towards the end of the star's life, the faster and stronger wind collides with the old gas masses along the star's equatorial plane. A shock front develops, and the fast outflowing gas masses are re-directed away from the equator, towards the poles. Two jets of gas arise, flowing away from the central star into opposite directions. From the symmetry of the physical system, and also probably amplified by the central star's magnetic field which additionally focuses the flow of photo-ionized gas plasma, the gas jets cannot do anything else but be axisymmetric, creating a bipolar shape [26].

In extensive gas-dynamic [19] and photo-ionization simulations [26, 21] the plausibility of the interactive winds theory has been demonstrated. On this basis, a low-dimensional (4 degrees of freedom) shape model for PNe, the *prolate ellipsoidal shell* (PES) model, was proposed by Masson [4] which was subsequently used by Kwok et al. [27, 28] to model the general appearances of a number of PNe. However, their simple geometrical model can only give a rough qualitative account of the spatial density distribution of the gas within PNe, and model fitting is a manual process.

4 Constrained Inverse Volume Rendering

The physical characteristics described above allow us to develop a method for automatically reconstructing the actual spatial gas distribution within PNe from conventional images.

4.1 The Model

Our *constrained inverse volume rendering* (CIVR) approach is based on three physical and observational properties:

- The axisymmetry of bipolar PNe simplifies the reconstruction by reducing the 3D nebula volume to a 2D local emission density function of cylindrical

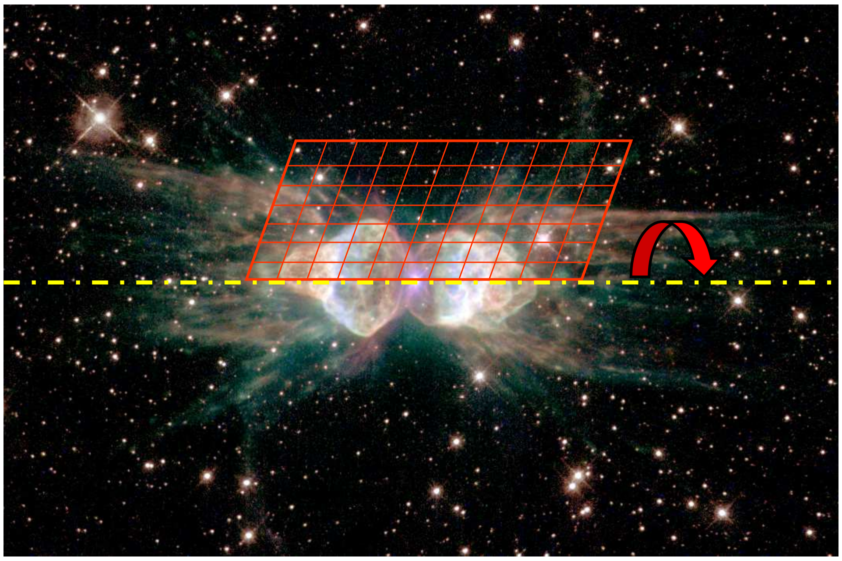

Figure 2: Axial symmetry: the 3D gas structure of planetary nebulae can be described by a density map in cylindrical coordinates. The volumetric density distribution in 3D space is generated by rotating the density map along the nebula's axis of symmetry (yellow).

coordinates.

- Scattering and absorption is neglected.
- Planetary nebula span only a few arc minutes in the sky (less than a tenth of a degree), so their projected appearance is essentially orthographic.

Our model consists of a two-dimensional density map whose entries represent axisymmetric emission density values. The map is aligned with the symmetry axis of the nebula such that the central star is in the middle, Fig.2. The CIVR algorithm determines all map values such that the corresponding projection image, obtained by rotating the density map around the symmetry axis and integrating emission density along the line of sight, matches the nebula's photograph.

Unfortunately, the relationship between axisymmetric density map entries and the nebula's projection image remains non-linear, since we don't know the nebula's angle of inclination and also because the map values may not become negative. We therefore pursue a non-linear optimization approach that relies extensively on evaluating an error functional that measures the difference between the projected PN model and the photo of its celestial counterpart. Thanks to fast volume rendering with modern graphics hardware, this error functional can be calculated extremely efficiently.

4.2 Volume Rendering and Error Evaluation

Since PNe consist of glowing gas, synthesizing faithful projection images from our PN model consists rendering a purely emissive volume. Implemented on PC graphics hardware, we render multiple viewport-aligned slices through the nebula volume at different depths [9]. A fragment program transforms rasterization coordinates to axisymmetric cylinder coordinates and performs the bilinearly interpolated look-up into the current 2D density map. For slice summation, we exploit the floating point buffer of modern graphics hardware. An nVidia GeForce FX 3000 graphics card easily attains 10 fps when rendering 128 slices at 128x128 image resolution.

To evaluate the projection error of current density map values, the floating point rendering result is compared pixel-wise to the original PN image. Our experiments found that a simple sum-of-squared-differences measure yields fast convergence results. In addition, the image error is made artificially high whenever the optimization routine produced a negative density value. This allows the otherwise generic optimization routine to be constrained to a physically plausible density model.

4.3 Optimization

The combination of a particular emission density map and the PN's orientation angles constitute one point in high-dimensional model space. The PN model is optimized by traversing the model space to minimize the error functional. We used a standard implementation of Powell's method [29], based on conjugate-gradient descent. The algorithm evaluates the error value at a number of locations around the current model in order to determine the incremental update that will decrease the error. Each error functional evaluation entails modifying the density map entries and orientation angle values, uploading them to the graphics card, generating the volume rendering, and calculating the per-pixel differences. This evaluation-optimization loop iterates until the algorithm converges to a minimum of the error function. As described in Sect.5.2, the optimization strategy also benefits from a multi-resolution approach, in which coarse models are optimized as starting points for higher-resolution models.

5 Reconstruction of Planetary Nebulae

This section describes the over-all procedure to reconstruct planetary nebulae and their orientation as seen from Earth.

5.1 Pre-processing

Our constrained inverse volume rendering (CIVR) method is based on conventional images of planetary nebulae (PNe). Research-grade images of many PNe are publicly available on the Internet. The data used for our work, and the astronomical images shown in the here, are from the Hubble Space Telescope Archive [24] and the IAC Morphological Catalog of Northern Galactic Planetary Nebulae [25].

Prior to applying our CIVR volume modeling method, the image must be preprocessed to correct for a number of imaging-related effects to obtain scientifically accurate data. For our CIVR technique to produce correct results, we need images that are linearly calibrated, i.e. doubling the number of photons falling on a pixel must double the pixel value. We calibrate the raw image data using the standard astronomical image processing software IRAF [30] and STSDAS [31].

Stars nearby and behind the nebula interfere with the reconstruction process because their light originates outside the nebula model. We manually mask out the regions around such stars. To avoid bias in the reconstruction result, the CIVR algorithm disregards these regions when computing the error functional; the masked pixels are effectively missing from the image. Due to imaging noise, the background pixels in the PN images additionally exhibit a small non-zero value. This is a second potential source of inaccuracy since the CIVR algorithm would attempt to model the light from behind the nebula as part of the nebula itself. Thus, we threshold the images and set the background uniformly to zero.

Finally, the PN's central star is identified in each image, and the nebula's projected line of symmetry is approximately determined. This can be done automatically by finding the maximum pixel value in the image or by determining the nebula pixels' center of gravity, and by calculating the principal eigenvectors of the image's covariance matrix. The PN image is centered on the central star and clipped to 256x256 pixels, which is sufficiently large to completely accommodate the nebulae in all our test images.

5.2 Volumetric Modeling

We now apply our CIVR algorithm to each calibrated image individually. Initially, all density map entries are set to zero. Because the nebula's symmetry axis goes through the central star, we initialize one orientation angle based on the slope of the PN's line of symmetry in the image. The second, unknown angle, representing the inclination of the nebula's symmetry axis towards Earth, is initialized to zero. The values of both angles are optimized during CIVR.

PNe are small objects in the sky, and atmospheric turbulence typically limits imaging resolution from ground-based telescopes to only a couple of hundred pixels along the longest dimensions. To determine at which resolution our axisymmetric density map may be optimally reconstructed, we rely on the Nyquist theorem that the highest measurable frequency corresponds to 2 samples per period. Thus, for a nebula covering 256 pixels in the image along its longest direction, we can recover 128 pixels for our density map.

To accelerate convergence, our CIVR implementation follows a multi-resolution approach. Reconstruction starts with a low-resolution version of the density map and image. At this level, only a fraction of density map entries must be reconstructed, and the model is volume-rendered very quickly also at low resolution. After convergence, the reconstructed low-resolution density map is scaled up to serve as initialization for the next-higher resolution density map. When increasing density map resolution, rendering resolution must increase likewise, which in turn increases rendering times during error function evaluation. Employing four hierarchy levels, reconstruction of a 128x32-pixel density map on a 2.4 GHz PC, in conjunction with an nVidia GeForce FX 3000 graphics card, takes approximately one day.

6 Results

PN	incl. angle	orient. angle
He2-437	$84^\circ/96^\circ$	77.5°
M1-92	$79^\circ/101^\circ$	16.5°
Mz-3	$55^\circ/125^\circ$	175.5°

Table 1: Reconstructed nebula orientations. The inclination angle can only be determined up to a symmetry ambiguity with respect to the perpendicular 90° orientation.

We evaluated our CIVR algorithm using three different PNe. For each nebula, we reconstructed the spatial emission distribution for a number of chemical elements, Fig.5. Fig4 shows color composites of the actual PN images alongside with renderings from the same viewpoint obtained from the reconstructed models and visualizations of iso-density surfaces within the nebulae. The volume renderings in the third column use multiple soft isosurfaces of the gas density to help convey the 3D structure of the PNe. The coloring on the isosurface comes from a volume RGB texture generated similarly to the images described in the next Section. Diffuse shading aids in interpreting 3D shape. In addition to the emission density maps, the orientation angles of each nebula are determined, Tab.1. Note that the orthographic projection property implies that the inclination angle can only be recovered ambiguously, giving two symmetrical solutions with respect to the perpendicular orientation. However, by assuming an equatorial dust belt around the central star, this symmetry can be broken, and the dimmer of either lobe must be behind the absorbing dust, visible e.g. for M1-92 in Fig.4.

6.1 Realistic Rendering

Our reconstructed PN models enable us to accurately visualize these attractive objects from arbitrary viewpoints. This is of value for planetarium shows and other educational purposes. To achieve the most natural visual impression, we wish to render the nebulae in accurate colors.

6.1.1 Color

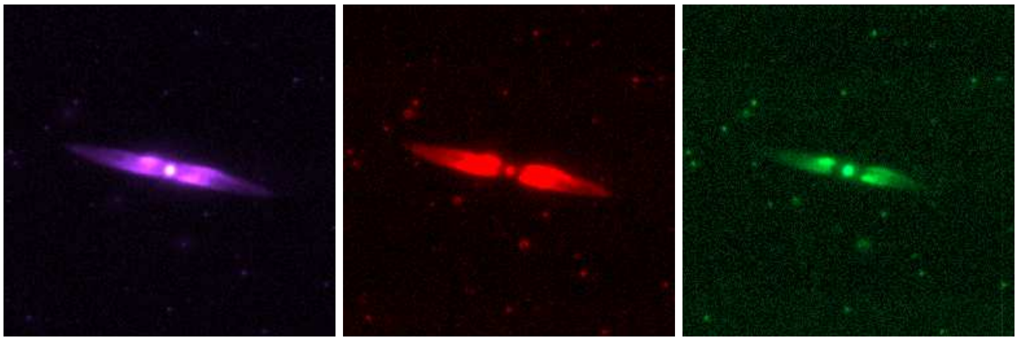

Figure 3: Input images: The planetary nebula He2-437 in the light of hydrogen, nitrogen and oxygen (from left to right). While the original image data is scalar-valued (grey-scale images), correct color appearance is determined by taking into account the complete emission line spectrum of each chemical element (Sect.6.1).

For the nebulae depicted in the paper, we made an effort to reproduce their actual colors. For each PN, we have available images corresponding to one characteristic emission line of the elements hydrogen, oxygen, and nitrogen or sulfur, Fig.3. These are the elements responsible for the visible color appearance of PNe. We assume that the images have been obtained using narrow-band filters which single out only the respective element's emission line. Tab.2 depicts all relevant emission lines in the visible region of the spectrum and their relative intensities. While relative emission line strengths are somewhat dependent on the physical conditions inside the nebula (temperature, electron density), we have adopted here mean values for PNe as published in the literature [22, 23] Having rendered a view using all elements' density maps, for each pixel we construct its emission spectrum according to its element emissions' intensities, Tab.2, which we convert to RGB values using the CIE 1931 XYZ color matching function values and the appropriate color space transformation [32].

element	wavelength	rel. line strength
hydrogen	656nm	1.
	486nm	0.365
	434nm	0.174
	410nm	0.096
oxygen	501nm	1.
	496nm	0.344
	436nm	0.014
nitrogen	658nm	1.
	655nm	0.33
	575nm	0.049
sulfur	673nm	1.
	672nm	0.57
	407nm	0.6

Table 2: Nebula colors: Planetary nebulae get their colorful appearance from a handful of discrete emission lines. The table depicts emission line wavelengths for the relevant elements with their relative intensities. By imaging the nebula at one wavelength for each element, the intensities of the other emission lines can be deduced (last column), and the nebula can be rendered in correct colors.

6.1.2 HDR Rendering

Planetary nebula images exhibit a high dynamic range. While the central star typically represents the brightest region in any PN image, the outermost regions of glowing gas frequently drown in detector noise. To simultaneously display the bright regions and the faint structure of the gas, we employ gamma correction to all three color channels. More advanced tone mapping operators may yield visually even more attractive rendering results [33].

Fig.6 depicts our planetary nebulae as seen under different inclination angles, corresponding to viewpoints located thousands of light years from Earth. Fly-around video sequences are also accessible at *http://www.mpi-sb.mpg.de/~magnor/civr.html*. Notice the considerable change in appearance with orientation angle, but also the diversity among different planetary nebulae.

6.2 Axisymmetric Gas Density Distribution

For each planetary nebula, we have available several images taken at different wavelengths, corresponding to different chemical elements, Fig.3. Separate density maps are reconstructed, showing the elements' spatial abundances in the nebulae, Fig.5. By rotating the density maps along their upper border, the three-dimensional emission distribution is constructed.

An astrophysical interpretation of the reconstructed axisymmetric maps must be done with great care. Especially our neglicence to absorption in and around the nebula may lead to systematic errors. This is obvious for M1-92 in Fig.4 where the southern lobe appears much darker than the northern lobe probably due to an equatorial belt of absorbing dust around the central star. Ideas how to improve the model to also incorporate the dust component of PNe will be mentioned in the last section.

It is noticeable that emission density appears to vary considerably within each nebula, indicating that the gas is distributed inhomogeneously. In addition, concentration maxima of different chemical elements seem to located in different regions. Finally, spatial distribution differs substantially between PNe. In He2-437, large regions of empty space seem to be present within the nebula. M1-92, in contrast, features two very different gas lobes with small, localized density concentrations along the axis of symmetry. The distribution in Mz-3 is even more complex, with most emission being concentrated along the shock front.

7 Discussion

The CIVR method reconstructs the axisymmetric structure of PNe such that the re-projection is a very close match to the actual, recorded image. In the following, we validate the credibility of CIVR results and discuss the inherent limitations of our reconstruction approach.

7.1 Validation

Since our optimization problem is non-linear, a proof for general convergence to the global minimum of our error function cannot be given. To validate the reconstruction results derived for real nebulae, we would have to know their actual 3D gas distribution. There exists a rather involved observation technique known as echellogrametry to reconstruct 3D gas velocities from which the 3D shape can be inferred. However, results have been published only for thin-shell spherical PNe so far [16, 17], which represents a rather simple case for CIVR.

Instead, we rely on synthetic images to test our approach. We make use of Kwok's ellipsoid shell model [27] to generate test images for a number of different orientations. We then let our CIVR algorithm recover the axisymmetric density distribution and orientation angles and compare the reconstructed values with the original values derived from the ellipsoid shell model. For inclination angles down to 40 degrees, the reconstructed map values are within the error range that is to be expected from the optimization routine's preset termination error threshold. The accuracy of the recovered inclination angle varies with angle value, from about 3° error for 90-degree inclination down to less than half a degree at 45° inclination. While we cannot test all possible cases, the validation experiments indicate that CIVR reconstruction results do, indeed, reflect the true 3D structure of planetary nebulae.

7.2 Limitations

For CIVR to produce reliable results, its three underlying assumptions must be fulfilled: The nebula is seen under almost orthographic projection, the gas distribution is by-and-large axisymmetric, and absorption and scattering at visual wavelengths is negligible. The first assumption's validity is established by the small apparent size of the nebula. The axisymmetric property originates from the interstellar conditions around the PN's central star. The last assumption, unfortunately, is not always valid. The equatorial gas belt around the central stars can exhibit substantial amounts of dust which scatters and absorbs light [34, 35].

CIVR can be applied not only to bipolar PNe, but also to spherical and point-symmetric PNe by incorporating point-symmetry into the model. Only for irregularly shaped nebulae, e.g. if the outflowing gas collides with interstellar gas clouds, our approach is not applicable.

CIVR works best for nebulae seen at high inclination angles, i.e. for PNe whose axis of symmetry is oriented approximately perpendicular to our viewing direction. This can be understood by approximating the reconstruction as an inverse linear problem and looking at the projection matrix' condition number. With decreasing inclination angle, i.e. when the PN's symmetry axis gets closer to our viewing direction, the matrix condition number increases and the (unregularized) reconstruction result becomes unstable. At 0° inclination, the symmetry axis points directly towards us, and the nebula's axial symmetry is of no use to constrain the reconstruction problem: the linear system of equations is underdetermined. Our validation experiments indicate that CIVR is capable of robustly reconstructing PNe down to inclination angles of 40°.

8 Conclusions

We have presented a constrained inverse volume rendering (CIVR) approach to recover the three-dimensional distribution of the photo-ionized gas in planetary nebulae (PNe) from conventional images. Thanks to their inherent axial symmetry, we are able to use an axisymmetric model to describe the nebula's emission distribution in space, thereby constraining the reconstruction problem. Being purely emissive, the PN model is volume-rendered efficiently using modern PC graphics hardware. By comparing the rendering result with the actual image, an optimization algorithm varies local emission as well as viewing direction to match the rendered model to the recorded image.

From the reconstructed 3D structure, planetary nebulae can be realistically viewed from arbitrary viewpoints. Applications include creating realistic visualizations of PNe as illustration material for astronomy courses, science programs, and planetarium shows.

In the future, the reconstruction method is hoped to be extendable to have value also for astrophysical research. The recovered 3D information may be used for studying the spatial relationship of element abundances in planetary nebulae, as well as to validate and refine the interacting winds theory. The reconstruction results may serve as input to drive coupled photo-ionization and gas-dynamic simulations [20] in order to create astrophysical physical models consistent with observations of actual planetary nebulae. It is conceivable that a general evolutionary sequence may be established among observed PNe that explains variation in composition and appearance based on only a handful of physical properties of the central star. Apart from planetary nebulae, there are other astronomical objects that exhibit axial symmetry, e.g. black holes ejecting opposite jets. Since the jets' synchrotron radiation is also thin, CIVR may be directly applied to radio observations to reconstruct electron density and magnetic field strength within those jets.

There are several ways how the presented CIVR method may be refined. First and foremost, the dust component may be taken into account. By assuming that dust is present mainly in the central star's equatorial plane, radial dust concentration can recovered for inclined PNe, also breaking the symmetry in inclination angle. Additionally, the ratio of hydrogen emission line intensities can serve as an indicator for dust along the line of sight. We have not yet made use of regularization, and did not enforce smoothness in our reconstructed density maps. This can be easily incorporated into our energy function. For noisy images, or if the nebula is only approximately axisymmetric, such additional constraints stabilize reconstruction. Another intriguing extension yielding visually even more attractive results consists of reconstructing the 3D structure in two steps; after the general axisymmetric structure has been recovered, remaining differences between the rendered model and the image may be attributed to emission density variations located on the nebula's shock front surface. This is plausible since small-scale density variations are most probably due to turbulence along the fast stellar wind's shock front. This way, non-axisymmetric details present in the PN images can be incorporated into the 3D model to be replicated during visualization.

References

[1] H. Curtis. The planetary nebulae. *Publ. Lick Observatory, part III*, (13):57–74, 1918.

[2] G. Khromov and L. Kohoutek. Morphological study of planetary nebulae. In D. Osterbrock and C. O'Dell, editors, *Planetary Nebulae*, pages 227–235. IAU Symposium 34, 1968.

[3] B. Balick. The evolution of planetary nebulae. I - structures, ionizations, and morphological sequences. *Astronomical Journal*, 94:671–678, September 1987.

[4] C. Masson. The structure of and distances to BD + 30 deg 3639 and NGC 6572. *Astrophysical Journal*, 346:243–250, 1989.

[5] B. Curless and M. Levoy. A volumetric method for building complex models from range images. *Proc. ACM SIGGRAPH (Computer Graphics Series)*, 30:303–312, 1996.

[6] K. Mueller, R. Yagel, and J.J. Wheller. A fast and accurate projection algorithm for the algebraic reconstruction technique (ART). *SPIE Medical Imaging Conference,* San Diego, USA, SPIE 3336:724–732, February 1998.

[7] S. Marschner. *Inverse Rendering for Computer Graphics*. PhD thesis, Cornell University, 1998.

[8] M. Levoy. Display of surfaces from volume data. *IEEE Computer Graphics and Applications*, 8(5):29–37, 1988.

[9] B. Cabral, N. Cam, and J. Foran. Accelerated volume rendering and tomographic reconstruction using texture mapping hardware. *Proc. Symposium on Volume Visualization (VolVis'94)*, pages 91–98, 1994.

[10] C. Rezk-Salama, K. Engel, M. Bauer, G. Greiner, and T. Ertl. Interactive volume rendering on standard PC graphics hardware using multi-textures and multi-stage rasterization. *Proc. ACM SIGGRAPH/EUROGRAPHICS Workshop on Graphics Hardware*, pages 109–118, 2000.

[11] N. Max. Optical models for direct volume rendering. *IEEE Trans. Visualization and Computer Graphics*, 1(2):99–108, 1995.

[12] D. Nadeau, J. Genetti, S. Napear, B. Pailthorpe, C. Emmart, E. Wesselak, and D. Davidson. Visualizing stars and emission nebulae. *Computer Graphics Forum*, 20(1):27–33, March 2001.

[13] J. Genetti. Volume-rendered galactic animations. *Communications of the ACM*, 45(11):62–66, November 2002.

[14] W. Zheng and C. O'Dell. A three-dimensional model of the Orion nebula. *Astrophysical Journal*, 438(2):784–793, January 1995.

[15] S. Kwok, C. Purton, and P. Fitzgerald. On the origin of planetary nebulae. *Astrophysical Journal*, 219:L125–L127, 1978.

[16] F. Sabbadin. Spatiokinematic models of five planetary nebulae. *Monthly Notices of the Royal Astronomical Society*, 210:341–358, 1984.

[17] F. Sabbadin, E. Cappellaro, S. Benetti, M. Turatto, and C. Zanin. Tomography of the low excitation planetary nebula NGC 40. *Astronomy & Astrophysics*, 355:688–698, March 2000.

[18] W. Saurer. Morphology and expansion characteristics of the planetary nebula M 1-79. *Astronomy & Astrophysics*, 326:1187–1194, October 1997.

[19] C. Mellema and A. Frank. Radiation gasdynamics of planetary nebulae - V. hot bubble and slow wind dynamics. *Monthly Notices of the Royal Astronomical Society*, 273:401–410, 1989.

[20] B. Armsdorfer, S. Kimeswenger, and T. Rauch. Effects of Central Star Models on Planetary Nebulae Shell Modelling. In *Ionized Gaseous Nebulae. Mexico City November 21- 24, 2000*, November 2000.

[21] C. Ercolano, C. Morisset, M. Barlow, P. Storey, and X.-W. Liu. Three-dimensional photoionization modelling of the planetary nebula NGC 3918. *Monthly Notices of the Royal Astronomical Society*, 340:1153–1172, 2003.

[22] D. Osterbrock. *Astrophysics of Gaseous Nebulae and Active Galactic Nuclei*. University Science Books, Sausalito, CA, 1989.

[23] S. Kwok. *The Origin and Evolution of Planetary Nebulae*. Cambridge University Press, Cambridge, UK, 2000.

[24] Hubble, 2004. http://archive.stsci.edu/hst/search.php.

[25] IAC, 2004. http://www.iac.es/nebu/nebula.html.

[26] C. Morrisset, R. Gruenwald, and S.M. Viegas. Morphology and kinematics of planetary nebulae. I a new modeling tool. *Astrophysical Journal*, 533:931–937, April 2000.

[27] O. Aaquist and S. Kwok. Radio morphologies of planetary nebulae. *Astrophysical Journal*, 462(2):813–824, May 1996.

[28] C. Zhang and S. Kwok. A morphology study of planetary nebulae. *Astrophysical Journal Supplement Series*, 117(2):341–359, August 1998.

[29] W. Press, B. Flannery, S. Teukolsky, and W. Vetterling. *Numerical Recipes in C*. Cambridge University Press, 1992.

[30] IRAF, 2004. http://iraf.tuc.noao.edu.

[31] STSDAS, 2004. www.stsci.edu/resources/software_hardware/stsdas.

[32] Günter. Wyszecki and Walter S. Stiles. *Color Science: Concepts and Methods, Quantitative Data and Formulae*. John Wiley & Sons, New York, 2nd edition, 1982.

[33] E. Reinhard, M. Stark, P. Shirley, and J. Ferwerda. Photographic tone reproduction for digital images. *ACM Trans. Graphics*, 21(3):267–276, 2002.

[34] H. E. Schwarz, C. Aspin, R. L. M. Corradi, and B. Reipurth. M 2-9: moving dust in a fast bipolar outflow. *Astronomy & Astrophysics*, 319:267–273, March 1997.

[35] H. E. Schwarz and H. Monteiro. Properties of Bipolar Planetary Nebulae. In *Revista Mexicana de Astronomia y Astrofisica Conference Series*, pages 23–28, January 2003.

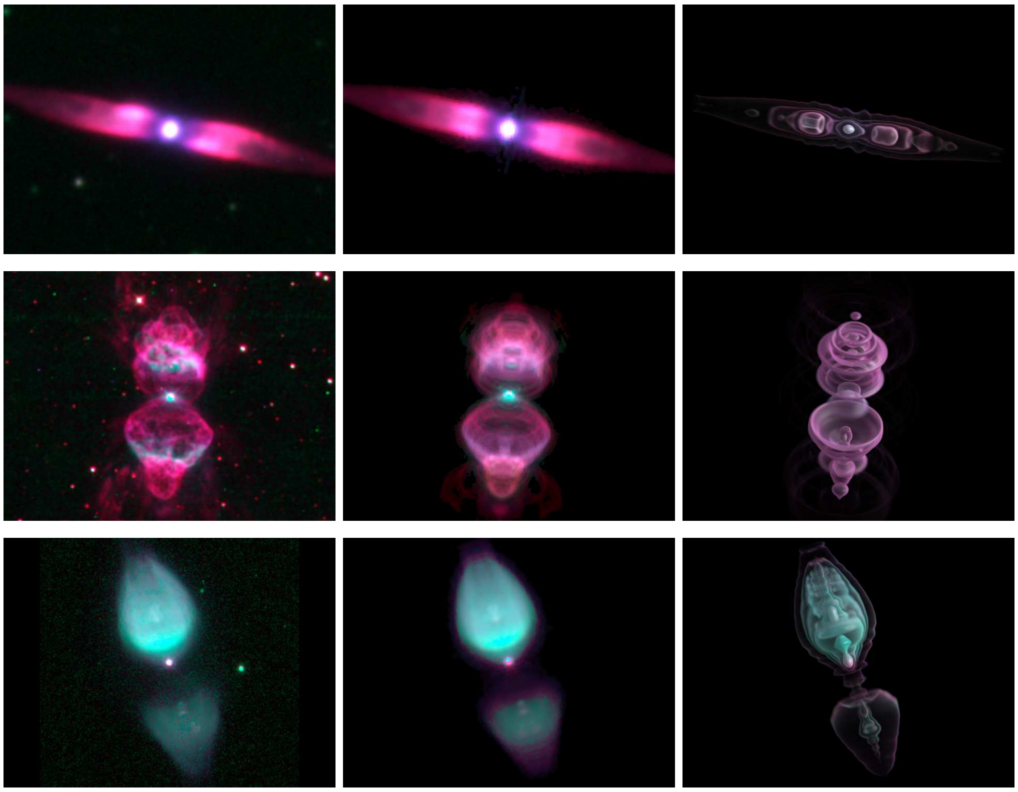

Figure 4: CIVR modeling results for the planetary nebulae He2-437 (top), Mz3 (middle) and M1-92 (bottom). Left to right: the color-composited original image, the same view rendered from the reconstructed model, and a visualization of the nebula's iso-density surfaces.

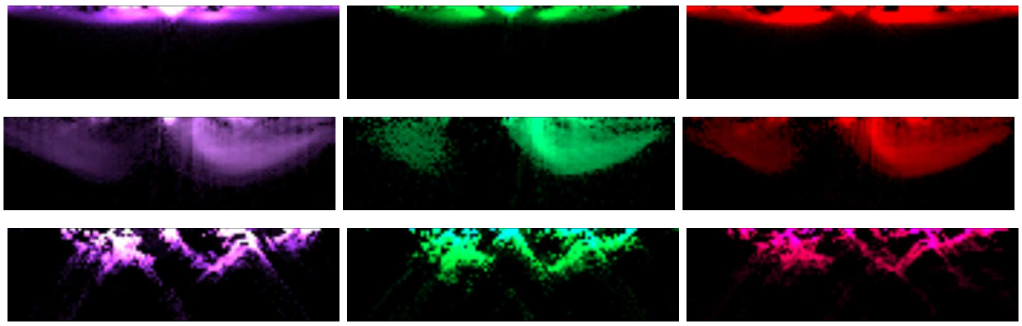

Figure 5: Axisymmetric structure of the planetary nebulae He2-437, M1-92, and Mz-3 (top to bottom). From left to right, the maps illustrate the distribution of the elements hydrogen, oxygen, and nitrogen (sulfur for Mz-3).

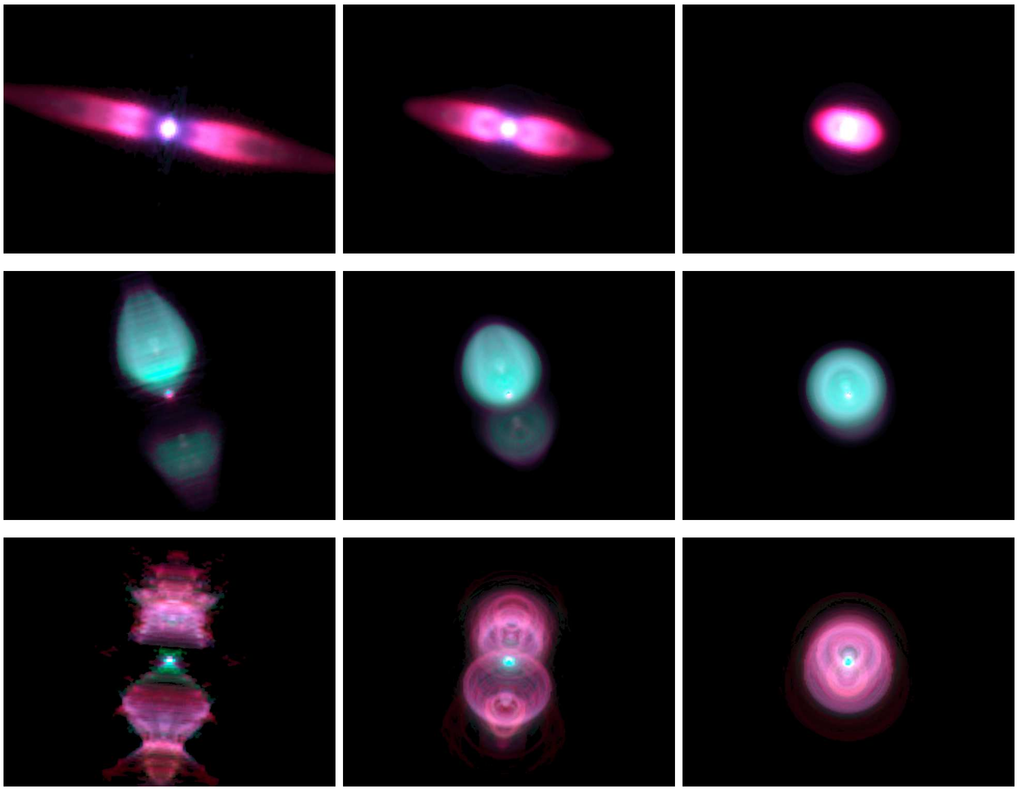

Figure 6: Unfamiliar views: He2-437, M1-92, and Mz-3 (top to bottom) as they would look at inclination angles of 85°, 35°, and 10° (left to right).

Below you find a list of the most recent technical reports of the Max-Planck-Institut für Informatik. They are available by anonymous ftp from `ftp.mpi-sb.mpg.de` under the directory `pub/papers/reports`. Most of the reports are also accessible via WWW using the URL `http://www.mpi-sb.mpg.de`. If you have any questions concerning ftp or WWW access, please contact `reports@mpi-sb.mpg.de`. Paper copies (which are not necessarily free of charge) can be ordered either by regular mail or by e-mail at the address below.

Max-Planck-Institut für Informatik
Library
attn. Anja Becker
Stuhlsatzenhausweg 85
66123 Saarbrücken
GERMANY
e-mail: `library@mpi-sb.mpg.de`

MPI-I-2004-NWG3-001	M. Magnor	?
MPI-I-2004-4-001	J. Haber, C. Schmitt, M. Koster, H. Seidel	Modeling Hair using a Wisp Hair Model
MPI-I-2004-2-001	H.d. Nivelle, Y. Kazakov	Resolution Decision Procedures for the Guarded Fragment with Transitive Guards
MPI-I-2004-1-003	I. Katriel	On Algorithms for Online Topological Ordering and Sorting
MPI-I-2004-1-002	P. Sanders, S. Pettie	A Simpler Linear Time 2/3 - epsilon Approximation for Maximum Weight Matching
MPI-I-2004-1-001	N. Beldiceanu, I. Katriel, S. Thiel	Filtering algorithms for the Same and UsedBy constraints
MPI-I-2003-NWG2-002	F. Eisenbrand	Fast integer programming in fixed dimension
MPI-I-2003-NWG2-001	L.S. Chandran, C.R. Subramanian	Girth and Treewidth
MPI-I-2003-4-009	N. Zakaria	FaceSketch: An Interface for Sketching and Coloring Cartoon Faces
MPI-I-2003-4-008	C. Roessl, I. Ivrissimtzis, H. Seidel	Tree-based triangle mesh connectivity encoding
MPI-I-2003-4-007	I. Ivrissimtzis, W. Jeong, H. Seidel	Neural Meshes: Statistical Learning Methods in Surface Reconstruction
MPI-I-2003-4-006	C. Roessl, F. Zeilfelder, G. Nrnberger, H. Seidel	Visualization of Volume Data with Quadratic Super Splines
MPI-I-2003-4-005	T. Hangelbroek, G. Nrnberger, C. Roessl, H.S. Seidel, F. Zeilfelder	The Dimension of C^1 Splines of Arbitrary Degree on a Tetrahedral Partition
MPI-I-2003-4-004	P. Bekaert, P. Slusallek, R. Cools, V. Havran, H. Seidel	A custom designed density estimation method for light transport
MPI-I-2003-4-003	R. Zayer, C. Roessl, H. Seidel	Convex Boundary Angle Based Flattening
MPI-I-2003-4-002	C. Theobalt, M. Li, M. Magnor, H. Seidel	A Flexible and Versatile Studio for Synchronized Multi-view Video Recording

MPI-I-2003-4-001	M. Tarini, H.P.A. Lensch, M. Goesele, H. Seidel	3D Acquisition of Mirroring Objects
MPI-I-2003-2-004	A. Podelski, A. Rybalchenko	Software Model Checking of Liveness Properties via Transition Invariants
MPI-I-2003-2-003	Y. Kazakov, H. Nivelle	Subsumption of concepts in $DL\ \mathscr{F}\mathscr{L}_0$ for (cyclic) terminologies with respect to descriptive semantics is PSPACE-complete
MPI-I-2003-2-002	M. Jaeger	A Representation Theorem and Applications to Measure Selection and Noninformative Priors
MPI-I-2003-2-001	P. Maier	Compositional Circular Assume-Guarantee Rules Cannot Be Sound And Complete
MPI-I-2003-1-018	G. Schaefer	A Note on the Smoothed Complexity of the Single-Source Shortest Path Problem
MPI-I-2003-1-017	G. Schfer, S. Leonardi	Cross-Monotonic Cost Sharing Methods for Connected Facility Location Games
MPI-I-2003-1-016	G. Schfer, N. Sivadasan	Topology Matters: Smoothed Competitive Analysis of Metrical Task Systems
MPI-I-2003-1-015	A. Kovcs	Sum-Multicoloring on Paths
MPI-I-2003-1-014	G. Schfer, L. Becchetti, S. Leonardi, A. Marchetti-Spaccamela, T. Vredeveld	Average Case and Smoothed Competitive Analysis of the Multi-Level Feedback Algorithm
MPI-I-2003-1-013	I. Katriel, S. Thiel	Fast Bound Consistency for the Global Cardinality Constraint
MPI-I-2003-1-012		- not published -
MPI-I-2003-1-011	P. Krysta, A. Czumaj, B. Voecking	Selfish Traffic Allocation for Server Farms
MPI-I-2003-1-010	H. Tamaki	A linear time heuristic for the branch-decomposition of planar graphs
MPI-I-2003-1-009	B. Csaba	On the Bollobás – Eldridge conjecture for bipartite graphs
MPI-I-2003-1-008	P. Sanders	Polynomial Time Algorithms for Network Information Flow
MPI-I-2003-1-007	H. Tamaki	Alternating cycles contribution: a strategy of tour-merging for the traveling salesman problem
MPI-I-2003-1-006	M. Dietzfelbinger, H. Tamaki	On the probability of rendezvous in graphs
MPI-I-2003-1-005	M. Dietzfelbinger, P. Woelfel	Almost Random Graphs with Simple Hash Functions
MPI-I-2003-1-004	E. Althaus, T. Polzin, S.V. Daneshmand	Improving Linear Programming Approaches for the Steiner Tree Problem
MPI-I-2003-1-003	R. Beier, B. Vcking	Random Knapsack in Expected Polynomial Time
MPI-I-2003-1-002	P. Krysta, P. Sanders, B. Vcking	Scheduling and Traffic Allocation for Tasks with Bounded Splittability
MPI-I-2003-1-001	P. Sanders, R. Dementiev	Asynchronous Parallel Disk Sorting
MPI-I-2002-4-002	F. Drago, W. Martens, K. Myszkowski, H. Seidel	Perceptual Evaluation of Tone Mapping Operators with Regard to Similarity and Preference

MPI-I-2002-4-001	M. Goesele, J. Kautz, J. Lang, H.P.A. Lensch, H. Seidel	Tutorial Notes ACM SM 02 A Framework for the Acquisition, Processing and Interactive Display of High Quality 3D Models
MPI-I-2002-2-008	W. Charatonik, J. Talbot	Atomic Set Constraints with Projection
MPI-I-2002-2-007	W. Charatonik, H. Ganzinger	Symposium on the Effectiveness of Logic in Computer Science in Honour of Moshe Vardi
MPI-I-2002-1-008	P. Sanders, J.L. Trff	The Factor Algorithm for All-to-all Communication on Clusters of SMP Nodes
MPI-I-2002-1-005	M. Hoefer	Performance of heuristic and approximation algorithms for the uncapacitated facility location problem
MPI-I-2002-1-004	S. Hert, T. Polzin, L. Kettner, G. Schfer	Exp Lab A Tool Set for Computational Experiments
MPI-I-2002-1-003	I. Katriel, P. Sanders, J.L. Trff	A Practical Minimum Scanning Tree Algorithm Using the Cycle Property
MPI-I-2002-1-002	F. Grandoni	Incrementally maintaining the number of l-cliques
MPI-I-2002-1-001	T. Polzin, S. Vahdati	Using (sub)graphs of small width for solving the Steiner problem
MPI-I-2001-4-005	H.P.A. Lensch, M. Goesele, H. Seidel	A Framework for the Acquisition, Processing and Interactive Display of High Quality 3D Models
MPI-I-2001-4-004	S.W. Choi, H. Seidel	Linear One-sided Stability of MAT for Weakly Injective Domain
MPI-I-2001-4-003	K. Daubert, W. Heidrich, J. Kautz, J. Dischler, H. Seidel	Efficient Light Transport Using Precomputed Visibility
MPI-I-2001-4-002	H.P.A. Lensch, J. Kautz, M. Goesele, H. Seidel	A Framework for the Acquisition, Processing, Transmission, and Interactive Display of High Quality 3D Models on the Web
MPI-I-2001-4-001	H.P.A. Lensch, J. Kautz, M. Goesele, W. Heidrich, H. Seidel	Image-Based Reconstruction of Spatially Varying Materials
MPI-I-2001-2-006	H. Nivelle, S. Schulz	Proceeding of the Second International Workshop of the Implementation of Logics